university of groningen

University Medical Center Groningen

University of Groningen

The information content of cosmic infrared background anisotropies

Reischke, Robert; Desjacques, Vincent; Zaroubi, Saleem

Published in:
Monthly Notices of the Royal Astronomical Society

DOI:
10.1093/mnras/stz3141

IMPORTANT NOTE: You are advised to consult the publisher's version (publisher's PDF) if you wish to cite from it. Please check the document version below.

Document Version
Publisher's PDF, also known as Version of record

Publication date:
2020

Link to publication in University of Groningen/UMCG research database

Citation for published version (APA):
Reischke, R., Desjacques, V., & Zaroubi, S. (2020). The information content of cosmic infrared background anisotropies. *Monthly Notices of the Royal Astronomical Society*, *491*(1), 1079-1092. https://doi.org/10.1093/mnras/stz3141

Copyright
Other than for strictly personal use, it is not permitted to download or to forward/distribute the text or part of it without the consent of the author(s) and/or copyright holder(s), unless the work is under an open content license (like Creative Commons).

The publication may also be distributed here under the terms of Article 25fa of the Dutch Copyright Act, indicated by the “Taverne” license. More information can be found on the University of Groningen website: https://www.rug.nl/library/open-access/self-archiving-pure/taverne-amendment.

Take-down policy
If you believe that this document breaches copyright please contact us providing details, and we will remove access to the work immediately and investigate your claim.

Downloaded from the University of Groningen/UMCG research database (Pure): http://www.rug.nl/research/portal. For technical reasons the number of authors shown on this cover page is limited to 10 maximum.

Download date: 04-05-2023

Monthly Notices
of the
ROYAL ASTRONOMICAL SOCIETY

MNRAS **491,** 1079–1092 (2020)
Advance Access publication 2019 November 20

doi:10.1093/mnras/stz3141

The information content of cosmic infrared background anisotropies

Robert Reischke [1,2]★ Vincent Desjacques[1] and Saleem Zaroubi[1,2,3]

[1]*Department of Physics, Technion, Haifa 32000, Israel*
[2]*Department of Natural Sciences, The Open University of Israel, 1 University Road, PO Box 808, Ra'anana 4353701, Israel*
[3]*Kapteyn Astronomical Institute, University of Groningen, Landleven 12, Groningen NL-9747AD, the Netherlands*

Accepted 2019 November 5. Received 2019 November 4; in original form 2019 September 9

ABSTRACT

We use analytic computations to predict the power spectrum as well as the bispectrum of cosmic infrared background (CIB) anisotropies. Our approach is based on the halo model and takes into account the mean luminosity–mass relation. The model is used to forecast the possibility to simultaneously constrain cosmological, CIB, and halo occupation distribution (HOD) parameters in the presence of foregrounds. For the analysis, we use wavelengths in eight frequency channels between 200 and 900 GHz with survey specifications given by `Planck` and `LiteBird`. We explore the sensitivity to the model parameters up to multipoles of $\ell = 1000$ using autocorrelation and cross-correlation between the different frequency bands. With this setting, cosmological, HOD, and CIB parameters can be constrained to a few per cent. Galactic dust is modelled by a power law and the shot-noise contribution as a frequency-dependent amplitude that are marginalized over. We find that dust residuals in the CIB maps only marginally influence constraints on standard cosmological parameters. Furthermore, the bispectrum yields tighter constraints (by a factor 4 in 1σ errors) on almost all model parameters, while the degeneracy directions are very similar to the ones of the power spectrum. The increase in sensitivity is most pronounced for the sum of the neutrino masses. Due to the similarity of degeneracies, a combination of both analysis is not needed for most parameters. This, however, might be due to the simplified bias description generally adopted in such halo model approaches.

Key words: large scale structure of the Universe – Infrared: galaxies.

1 INTRODUCTION

A good fraction of the radiation emitted by stars in galaxies is absorbed by dust and re-emitted in the far-infrared. The resulting diffuse background produced by distant galaxies is called the cosmic infrared background (CIB). Measurements of the CIB (e.g. Dwek et al. 1998; Fixsen et al. 1998; Planck Collaboration XVIII 2011) therefore provide a window into the galaxy formation history of the Universe. In addition to its dependence on the star formation rate (out to fairly high redshifts), the CIB also furnishes a probe of the cosmological background as well as fluctuations in the galaxy distribution. Therefore, it also carries a wealth of cosmological information.

Anisotropies in the CIB have drawn a lot of attention since they have been detected, e.g. by Lagache et al. (2007), Viero et al. (2009), Hall et al. (2010), and Viero et al. (2012) in the range 100−1000 μm or in the submilimeter. Planck Collaboration XVIII (2011) measured the CIB anisotropies with unprecedented accuracy, which since then has been updated and also cross-correlated with the lensing potential of the cosmic microwave background (CMB; Planck Collaboration XXX 2014). At the same time, the theoretical modelling of the anisotropies underwent a lot of activities. While early models fitted biased linear power spectra (Lagache et al. 2007; Hall et al. 2010), these models have been replaced by more elaborate ones (Planck Collaboration XVIII 2011). Current models consist of two ingredients: a description of the evolution of the dark matter distribution and a model for the evolution of the galaxies that reside in the ambient dark matter as well as the connection between both. For the galaxies, many models have been used that reproduce the observed differential number counts and luminosity functions (e.g. Béthermin et al. 2011). The halo model (Cooray & Sheth 2002) in combination with the halo occupation distribution (HOD) offers a framework to study the spatial distribution of galaxies by linking the number of galaxies in a specific halo to its mass. This model was used by several authors to study the power spectrum and the bispectrum of the CIB (Viero et al. 2009; Pénin et al. 2012; Lacasa,

★ E-mail: r.reischke@campus.technion.ac.il

© 2019 The Author(s)
Published by Oxford University Press on behalf of the Royal Astronomical Society

Downloaded from https://academic.oup.com/mnras/article-abstract/491/1/1079/5634281 by University of Groningen user on 03 July 2020

Pénin & Aghanim 2014; Pénin, Lacasa & Aghanim 2014) and to put forecasts on constraints on the HOD parameters. Shang et al. (2012) proposed an improved model to capture the mass dependence of the mean mass–luminosity relation in case of the CIB's power spectrum. Both models where used to fit the CIB measured by the *Planck* satellite (Planck Collaboration XXX 2014). Wu & Doré (2017) constructed an empirical model including stellar mass functions, the star-forming main sequence as well as dust attenquation. Recently, the CIB has also been used to constrain star formation rates or dark energy (Maniyar, Béthermin & Lagache 2018; Maniyar et al. 2019).

Owing to their extended redshift range, measurements of the far-CIB (like other intensity mappings) probe comoving volumes significantly larger than those accessible to forthcoming galaxy surveys (such as *Euclid* or LSST). On the other hand, they are mainly limited by contamination of the dust of the Milky Way. It is therefore necessary to either remove the galactic dust from the CIB maps or model it accordingly and marginalize over the dust component in the end. Thus, provided the foreground can either be removed or modelled, the anisotropies of the CIB can in principle be used to constrain HOD and cosmological parameters. Tucci, Desjacques & Kunz (2016) showed for example how the power spectrum of the CIB anisotropies can potentially constrain local primordial non-Gaussianities at a level competitive with future galaxy surveys.

In this work, we use the formalism developed in Lacasa et al. (2014) to extend the model described in Shang et al. (2012) to the bispectrum. We only model the at least partially connected parts of the spectra using the halo model. The purely disconnected parts, i.e. the shot-noise component, are treated as free parameters in the analysis to fit the angular spectra at high multipoles. We then study the impact of foregrounds given by galactic dust that we model by a power law for the spatial part and by a modified blackbody spectrum for the frequency dependence. The impact of residual foregrounds is investigated for the power spectrum for a combined survey of the *Planck* and LiteBird frequencies above 200 GHz with a total of eight frequency channels by studying the constraints on CIB, HOD, and cosmological parameters. Including also the information of the bispectrum, we then compare its performance with the power spectrum analysis and also give the joint constraints between both probes. If not stated otherwise, we will use the best-fitting CIB parameters from Planck Collaboration XXX (2014) and the best-fitting cosmological parameters of Planck Collaboration (2018).

The remainder of the paper is structured as follows: In Section 2, we review the modelling of CIB anisotropies and give the explicit expressions up to the bispectrum. Section 3 briefly introduces the statistical analysis. We show results in Section 4 and conclude in Section 5.

2 CIB ANISOTROPIES

In this section, we briefly review the modelling of CIB anisotropies on the basis of the halo model and the HOD. We provide the equations for the angular power spectrum and the bispectrum. Furthermore, we will briefly discuss the shot-noise component and galactic foregrounds.

2.1 CIB anisotropies

The specific infrared intensity at frequency ν is given by

$$I_\nu = \int \mathrm{d}\chi a j_\nu(\chi(z)) = \int \mathrm{d}\chi a \bar{j}_\nu(\chi(z)) \left(1 + \frac{\delta j_\nu(\chi(z))}{\bar{j}_\nu(\chi(z))}\right) , \tag{1}$$

where $j_\nu(\chi(z))$ is the specific emission coefficient and a bar indicates the average emissivity. We integrate along the line of sight over the comoving distance:

$$\chi(z(a)) = -c \int_1^a \frac{\mathrm{d}a}{a^2 H(a)} , \tag{2}$$

with the scale factor a and the Hubble function $H := \dot{a}/a$. Introducing a spherical basis, $\delta I_\nu = \sum_{\ell,m} \delta I_{\ell m,\nu} Y_{\ell m}$, the correlation of the spherical harmonic coefficients defines the angular power spectrum:

$$\left\langle \delta I_{\ell m,\nu} \delta I_{\ell' m',\nu'} \right\rangle = C_{\ell,\nu\nu'} \delta_{\ell\ell'} \delta_{mm'} , \tag{3}$$

where the Kronecker deltas, $\delta_{\ell\ell'}$ and $\delta_{mm'}$, ensure spatial homogeneity and isotropy, respectively. Using the Limber approximation (Limber 1954), the angular power spectrum can be calculated as

$$C_{\ell,\nu\nu'} = \int \frac{\mathrm{d}\chi}{\chi^2} a^2 \bar{j}_\nu(\chi(z)) \bar{j}_{\nu'}(\chi(z)) P_{j,\nu\nu'} \left(\frac{\ell + 0.5}{\chi}, \chi\right) , \tag{4}$$

with the power spectrum of the emission coefficient:

$$(2\pi)^3 \bar{j}_\nu(\chi(z)) \bar{j}_{\nu'}(\chi(z)) P_{j,\nu\nu'}(k, \chi) \delta_{\mathrm{D}}^{(3)}(\boldsymbol{k} - \boldsymbol{k}') = \langle \delta j_\nu(\boldsymbol{k}) \delta j_{\nu'}(\boldsymbol{k}') \rangle . \tag{5}$$

One can now equate $P_{j,\nu\nu'}$ with the power spectrum of galaxies. This assumes that spatial variations in the emission coefficient are sourced by galaxies, such that $\delta j_\nu / \bar{j}_\nu = \delta n_{\mathrm{gal}} / \bar{n}_{\mathrm{gal}}$ and that there are no other biases apart from the galaxy bias itself. The above procedure generalizes to higher order spectra. For the angular bispectrum defined by

$$\left\langle \delta I_{\ell_1 m_1,\nu_1} \delta I_{\ell_2 m_2,\nu_2} \delta I_{\ell_3 m_3,\nu_3} \right\rangle = \begin{pmatrix} \ell_1 & \ell_2 & \ell_3 \\ m_1 & m_2 & m_3 \end{pmatrix} B_{\nu_1,\nu_2,\nu_3}(\ell_1, \ell_2, \ell_3) , \tag{6}$$

Downloaded from https://academic.oup.com/mnras/article-abstract/491/1/1079/5634281 by University of Groningen user on 03 July 2020

where the Wigner 3j symbol was introduced. $B_{\nu_1,\nu_2,\nu_3}(\ell_1, \ell_2, \ell_3)$ can be expressed as follows, again using the Limber approximation

$$B_{\nu_1,\nu_2,\nu_3}(\ell_1, \ell_2, \ell_3) = \int \frac{\mathrm{d}\chi}{\chi^4} \bar{j}_{\nu_1}(\chi)\bar{j}_{\nu_2}(\chi)\bar{j}_{\nu_3}(\chi)a^3(\chi)B_{j,\nu_1\nu_2\nu_3}\left(\frac{\ell_1+0.5}{\chi}, \frac{\ell_2+0.5}{\chi}, \frac{\ell_3+0.5}{\chi}, \chi\right) , \tag{7}$$

with the bispectrum of the emissivity coefficient $B_{j,\nu_1\nu_2\nu_3}(k_1, k_2, k_3, \chi)$, given by

$$(2\pi)^3 \bar{j}_{\nu_1}(\chi(z))\bar{j}_{\nu_2}(\chi(z))\bar{j}_{\nu_3}(\chi(z))B_{j,\nu_1\nu_2\nu_3}(k_1, k_2, k_3, \chi)\delta_{\mathrm{D}}^{(3)}(\boldsymbol{k}_{123}) = \langle \delta j_{\nu_1}(\boldsymbol{k}_1)\delta j_{\nu_2}(\boldsymbol{k}_2)\delta j_{\nu_3}(\boldsymbol{k}_3)\rangle , \tag{8}$$

where $\delta_{\mathrm{D}}^{(3)}(\boldsymbol{k}_{123})$ ensures that the three wave vectors form a proper triangle. As for the power spectrum, we will relate the bispectrum of the emissivity coefficient to the galaxy bispectrum (equation 18).

2.2 Halo model

The connection between galaxies and dark matter can be described using the halo model together with the HOD. The galaxy power spectrum is generally given by

$$P_{\mathrm{gal}}(k, z) = P_{1\mathrm{h}}(k, z) + P_{2\mathrm{h}}(k, z) + P_{\mathrm{shot}}(k, z) , \tag{9}$$

with the one-halo, two-halo, and shot-noise term, respectively:

$$\begin{aligned} P_{1\mathrm{h}} &= \int \mathrm{d}M \frac{\mathrm{d}n}{\mathrm{d}M}(M, z)\frac{2N_{\mathrm{cen}}(M, z)N_{\mathrm{sat}}(M, z) + N_{\mathrm{sat}}^2(M, z)}{\bar{n}_{\mathrm{gal}}^2}u^2(k|M, z) , \\ P_{2\mathrm{h}} &= \left(\int \mathrm{d}M \frac{\mathrm{d}n}{\mathrm{d}M}(M, z)\frac{N_{\mathrm{cen}}(M, z) + N_{\mathrm{sat}}(M, z)}{\bar{n}_{\mathrm{gal}}}b_1(M, z)u(k|M, z)\right)^2 P_{\mathrm{lin}}(k, z) , \\ P_{\mathrm{shot}} &= \frac{1}{\bar{n}_{\mathrm{gal}}} . \end{aligned} \tag{10}$$

Here, dn/dM is the halo mass function for which we use the (Tinker et al. 2008) fitting formula and $P_{\mathrm{lin}}(k, z)$ is the linearly evolved matter power spectrum. $u(k|M, z)$ the Fourier transform of the density profile of a halo at given mass and redshift: The density profile of the haloes dictates the small-scale clustering properties of the galaxies. For an NFW halo (Navarro, Frenk & White 1997), the Fourier transform of the density profile is given by

$$u(k|M, z) = \cos(kr_{\mathrm{s}})\left[\mathrm{Ci}(k(1+c)r_{\mathrm{s}}) - \mathrm{Ci}(kr_{\mathrm{s}})\right] - \frac{\sin(ckr_{\mathrm{s}})}{kr_{\mathrm{s}}(1+c)} + \frac{\sin(kr_{\mathrm{s}})\left(\mathrm{Si}(kr_{\mathrm{s}}(1+c)) - \mathrm{Si}(kr_{\mathrm{s}})\right)}{\frac{1}{1+c} + \ln(1+c) - 1} . \tag{11}$$

The concentration c is given by an empirical relation and the scaling radius is given by

$$r_{\mathrm{s}} = \frac{r_{\mathrm{vir}}}{c} = \left(\frac{3M}{4\pi\Delta_V\bar{\rho}_{\mathrm{m}}c^3}\right)^{1/3} , \tag{12}$$

with $\Delta_V = 200$, from the spherical collapse of dark matter haloes, and $\bar{\rho}_{\mathrm{m}}$ the average matter density. In particular, the virial radius, r_{vir}, is defined as the radius a sphere with the virial density, Δ_V, and mass M would have. The total mass is thus contained in the virial radius, avoiding divergencies when integrating the NFW profile over the whole space. $\bar{n}_{\mathrm{gal}}$ is the mean number density of galaxies defined as

$$\bar{n}_{\mathrm{gal}}(z) = \int \mathrm{d}M[N_{\mathrm{sat}}(M, z) + N_{\mathrm{cen}}(M, z)]\frac{\mathrm{d}n}{\mathrm{d}M}(M, z) . \tag{13}$$

In this expression, $N_{\mathrm{gal}}(M, z) = N_{\mathrm{sat}}(M, z) + N_{\mathrm{cen}}(M, z)$ is the average number of galaxies in haloes of mass M at redshift z. N_{cen} and N_{sat} denote the contribution from central and satellite galaxies, respectively. HODs suggest that the average number of satellite and central galaxies can be parametrized as follows:

$$N_{\mathrm{sat}}(M, z) = \frac{1}{2}\left[1 + \mathrm{erf}\left(\frac{\log_{10}(M) - \log_{10}(2M_{\mathrm{min}})}{\sigma_{\log_{10}M}}\right)\right]\left(\frac{M}{M_{\mathrm{sat}}}\right)^{\alpha_{\mathrm{sat}}} , \quad N_{\mathrm{cen}}(M, z) = \frac{1}{2}\left[1 + \mathrm{erf}\left(\frac{\log_{10}(M) - \log_{10}(M_{\mathrm{min}})}{\sigma_{\log_{10}M}}\right)\right] , \tag{14}$$

in which M_{min} and α_{sat} are determined by observations. In our model, we use the subhalo mass function, dN_{sub}/dm, which we take to be of the form (Tinker & Wetzel 2010)

$$\frac{\mathrm{d}N_{\mathrm{sub}}}{\mathrm{d}\ln m}(m|M) = 0.3\left(\frac{m}{M}\right)^{-0.7}\exp\left[-9.9\left(\frac{m}{M}\right)^{2.5}\right] , \tag{15}$$

where M and m are the mass of the parent halo and the subhalo, respectively. The number of satellite galaxies can then be computed as

$$N_{\mathrm{sat}}(M, z) = \int \mathrm{d}\ln m \frac{\mathrm{d}N_{\mathrm{sub}}}{\mathrm{d}\ln m}(m|M) . \tag{16}$$

Finally, the first-order bias, $b_1(\nu)$, is chosen such that the constraint (Tinker et al. 2008)

$$1 = \int \mathrm{d}\nu b_1(\nu)f(\nu) , \tag{17}$$

Downloaded from https://academic.oup.com/mnras/article-abstract/491/1/1079/5634281 by University of Groningen user on 03 July 2020

is fulfilled subject to the constraint of the mass function. In similar fashion, one finds for the bispectrum of galaxies in the halo model (e.g. Lacasa et al. 2014) the following relations:

$$B_{\rm gal}(k_1,k_2,k_3,z) = B_{1h}(k_1,k_2,k_3,z) + B_{2h}(k_1,k_2,k_3,z) + B_{3h}(k_1,k_2,k_3,z) + B_{\rm shot1h}(k_1,k_2,k_3,z) + B_{\rm shot2h}(k_1,k_2,k_3,z)\,, \tag{18}$$

where

$$\begin{aligned}
B_{1h}(k_1,k_2,k_3,z) &= \int {\rm d}M \frac{{\rm d}n}{{\rm d}M}(M,z) u(k_1|M,z)u(k_2|M,z)u(k_3|M,z)\frac{N^3_{\rm sat}(M,z)+3N_{\rm cen}(M,z)N^2_{\rm sat}(M,z)}{\bar{n}_{\rm gal}(z)}\,,\\
B_{2h}(k_1,k_2,k_3,z) &= \mathcal{G}_1(k_1,k_2,z)P_{\rm lin}(k_3,z)\mathcal{F}_1(k_3,z) + \mathcal{G}_1(k_1,k_3,z)P_{\rm lin}(k_2,z)\mathcal{F}_1(k_2,z) + \mathcal{G}_1(k_2,k_3,z)P_{\rm lin}(k_1,z)\mathcal{F}_1(k_1,z)\,,\\
B_{3h}(k_1,k_2,k_3,z) &= \mathcal{F}_1(k_1,z)\mathcal{F}_1(k_2,z)\mathcal{F}_1(k_3,z)\left[F_2(\boldsymbol{k_1},\boldsymbol{k_2})P_{\rm lin}(k_1,z)P_{\rm lin}(k_2,z) + {\rm perm}\right]\\
&\quad + \mathcal{F}_1(k_1,z)\mathcal{F}_1(k_2,z)\mathcal{F}_2(k_3,z)P_{\rm lin}(k_1,z)P_{\rm lin}(k_2,z) + {\rm perm}\,.
\end{aligned} \tag{19}$$

The following functions have been defined for shorthand convenience:

$$\begin{aligned}
\mathcal{F}_1(k,z) &= \int {\rm d}M \frac{N_{\rm gal}(M,z)}{\bar{n}_{\rm gal}(z)}\frac{{\rm d}n}{{\rm d}M}(M,z)b_1(M,z)u(k|M,z)\,,\\
\mathcal{F}_2(k,z) &= \int {\rm d}M \frac{N_{\rm gal}(M,z)}{\bar{n}_{\rm gal}(z)}\frac{{\rm d}n}{{\rm d}M}(M,z)b_2(M,z)u(k|M,z)\,,\\
\mathcal{G}_1(k_1,k_2,z) &= \int {\rm d}M \frac{2N_{\rm cen}(M,z)N_{\rm sat}(M,z)+N^2_{\rm sat}(M,z)}{\bar{n}^2_{\rm gal}}\frac{{\rm d}n}{{\rm d}M}(M,z)b_1(M,z)u(k_1|M,z)u(k_2|M,z)\,,\\
F_2(\boldsymbol{k_1},\boldsymbol{k_2}) &= \frac{5}{7} + \frac{1}{2}\cos(\theta_{12})\left(\frac{k_1}{k2}+\frac{k_2}{k_1}\right) + \frac{2}{7}\cos^2(\theta_{12})\,,
\end{aligned} \tag{20}$$

with the first- and second-order bias b_1 and b_2, respectively. The second-order bias is given by a fitting equation given by (Lazeyras et al. 2016)

$$b_2(\nu) = 0.412 - 2.143b_1 + 0.929b_1^2 + 0.008b_1^3\,. \tag{21}$$

The quantity ν describes the peak-background split threshold with $\nu = \delta_{\rm c}/\sigma(M,z)$. For the mass function, we take the (Tinker et al. 2008) and a consistent expression for the linear bias b_1. $\sigma(M,z)$ is the standard deviation of the density field smoothed at a mass scale

$$\sigma^2(M) = \frac{1}{2\pi^2}\int k^2{\rm d}k \left(\frac{j_1(kR(M))}{kR(M)}\right)^2 P_{\rm lin}(k)\,, \tag{22}$$

with the spherical Bessel function j_1 and

$$R^3(M) = \frac{3M}{4\pi\bar{\rho}_{\rm m}(a)}\,. \tag{23}$$

The linear power spectrum is calculated with CLASS (Lesgourgues 2011) assuming the fiducial cosmology outlined above.

2.3 Mean emissivity

Following Shang et al. (2012), we will sum up all galaxies contributing to the CIB luminosity at a given frequency and redshift weighted by their differential number density, i.e. the halo mass function:

$$\bar{j}_\nu(z) = \int {\rm d}M \frac{{\rm d}n}{{\rm d}M}\left[f^c_\nu(M,z) + f^s_\nu(M,z)\right]\,. \tag{24}$$

In particular, we split the mean emissivity into a contribution from central, $f^c_\nu(M,z)$, and satellite galaxies, $f^s_\nu(M,z)$ which can be calculated by

$$f^c_\nu(M,z) = \frac{1}{4\pi}N_c(M,z)L_{c,(1+z)\nu}(M,z), \quad f^s_\nu(M,z) = \frac{1}{4\pi}\int_0^M {\rm d}m \frac{{\rm d}N_{\rm sub}}{{\rm d}m}(m,z|M)L_{s,(1+z)\nu}(m,z)\,. \tag{25}$$

This definition ensures that the contribution to the total emissivity depends on the mass not only by the number density of sources at a given mass, but also on the mass–luminosity relation, which is encoded in $L_{(1+z)\nu}(M,z)$. For simplicity, the infrared luminosity is assumed to be the same for central and satellite galaxies:

$$L_{(1+z)\nu}(M,z) = L_0(1+z)^\delta \frac{M}{\sqrt{2\pi\sigma^2_{L/M}}}\exp\left[-\frac{\ln(M)-\ln(M_{\rm eff})}{2\sigma^2_{L/M}}\right]\Theta_{\rm CIB}[(1+z)\nu]\,. \tag{26}$$

However, this assumption can easily be relaxed and to separate emissivities can be introduced. In this case, both galaxy types would contribute differently to the observed intensity of the CIB not only by their different abundance but also due to their emission characteristics. The luminosity peaks at a halo mass $M_{\rm eff}$ around which the negative feedback from supernovae and active galactic nuclei on the star formation

Downloaded from https://academic.oup.com/mnras/article-abstract/491/1/1079/5634281 by University of Groningen user on 03 July 2020

Table 1. Best-fitting CIB and halo occupation parameters together with their description. The parameters are chosen to fit the power spectra measurements of the data from (Planck Collaboration XXX 2014).

Parameter	Fiducial value	Description
α	0.36	Exponent of the dust temperature's redshift dependence
T_0	24.4 K	Dust temperature today
β	1.75	Modification to the CIB's blackbody spectrum
γ	1.7	CIB's power-law emissivity at high frequencies
δ	3.6	Exponent of the CIB's normalization redshift evolution
$M_{\rm eff}$	$10^{12.6}\,{\rm M}_\odot$	Peak of the specific CIB emissivity
$\sigma^2_{L/M}$	0.5	Range of halo masses producing a certain emissivity
$M_{\rm c}$	$3\times10^{11}\,{\rm M}_\odot\,h^{-1}$	Minimum mass for a halo to host a central galaxy

rate is minimum. The overall amplitude L_0 is determined by fits to data. We will discuss this point further in Section 4. For the spectral energy distribution (SED) of the galaxies, we assume a modified blackbody spectrum with a power-law emissivity (e.g. Hall et al. 2010):

$$\Theta_{\rm CIB} = \begin{cases} \left(\frac{\nu}{\nu_0}\right)^{\beta} \frac{B_\nu(T_{\rm d})}{B_{\nu_0}(T_{\rm d})} & \nu \le \nu_0\,, \\ \left(\frac{\nu}{\nu_0}\right)^{\gamma} & \nu > \nu_0\,. \end{cases} \tag{27}$$

Here, B_ν is the Planck function and $T_{\rm d}$ is the dust temperature for which we assume the following redshift dependence:

$$T(z) = T_0(1+z)^{\alpha}\,. \tag{28}$$

The two regimes are smoothly connected at ν_0 such that

$$\frac{{\rm d}\log\Theta}{{\rm d}\log\nu} = -\gamma\,. \tag{29}$$

Replacing the relations (14) by (25) fully specifies the model and takes into account the mass dependence of the luminosity as described in Shang et al. (2012). The fiducial parameters of our model are summarized in Table 1.

2.4 Shot noise

As discussed in Shang et al. (2012), the model could in principle describe the shot-noise term (which could in principle absorb the constant low-ℓ piece of the one-halo term) originating from local fluctuations in the number density of galaxies. However, since this shot noise is mainly sourced by the scatter in the luminosity–mass relation, which is not included in expression (26), it will generally be underestimated by the model. In principle, there exist parametric models for the shot noise (Béthermin et al. 2011). Notwithstanding, we will remain agnostic and treat the shot-noise amplitude as a free parameter like, for example, in the analysis performed in Planck Collaboration XXX (2014). In Fig. 1, we show the CIB spectra as calculated for a Planck cosmology with the parameters from Table 1. The dashed blue line shows the clustering contribution, i.e. the sum of the one- and the two-halo term. In black, the shot noise level is shown, while the solid blue curves show the sum of all contributions. Furthermore, Fig. 2 shows the bispectrum at 353 GHz for different triangular configurations including only the clustering terms.

2.5 Galactic dust

The main foreground at infrared frequencies exceeding 200 GHz is the Galactic dust emission. Like the SED of the CIB, its frequency spectrum is also well described by a modified blackbody spectrum of the form (Planck Collaboration XXX 2014)

$$\Theta_{\rm d}(\nu) = \left(\frac{\nu}{\nu_0}\right)^{\beta_{\rm d}} \frac{B_\nu(T_{\rm d})}{B_{\nu_0}(T_{\rm d})}\,. \tag{30}$$

The reference frequency ν_0 is chosen to be 353 GHz. The best-fitting dust temperature (assumed to be constant for all galaxies) and spectral index are $T_{\rm d} = 19.6\,{\rm K}$, $\beta_{\rm d} = 1.53$. We split the dust power spectra into a spatial correlation and a frequency correlation:

$$C^{\rm d}_{\ell,\nu\nu'} = C^{\rm d}_\ell(\nu_0)\Theta_{\rm d}(\nu)\Theta_{\rm d}(\nu')R_{\nu\nu'}\,, \tag{31}$$

where the frequency correlation matrix $\boldsymbol{R}$ is given by (Tegmark 1998)

$$R_{\nu\nu'} = \exp\left[-\frac{1}{2}\left(\frac{\ln(\nu/\nu')}{\zeta}\right)^2\right]\,. \tag{32}$$

The frequency coherence ζ encodes the strength of the correlation such that for $\zeta \to 0$, $\boldsymbol{R} \to \mathbf{id}$, i.e. correlations between different frequency channels are absent. Conversely, $\zeta \to \infty$ corresponds to maximally correlated channels.

Downloaded from https://academic.oup.com/mnras/article-abstract/491/1/1079/5634281 by University of Groningen user on 03 July 2020

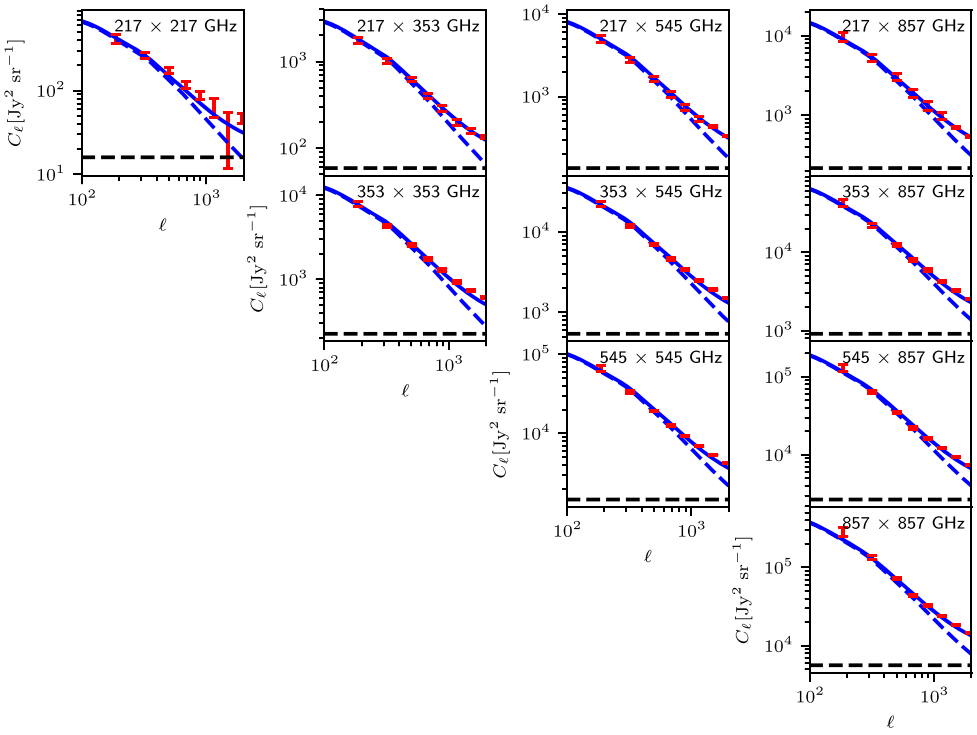

Figure 1. CIB anisotropy angular power spectra as measured by Planck Collaboration XXX (2014) in four frequency bands. The data points are shown in red. The dashed blue line corresponds to the clustering contribution, while the dashed black line shows the shot noise contribution in each band. In solid blue, we show the sum of clustering and shot noise.

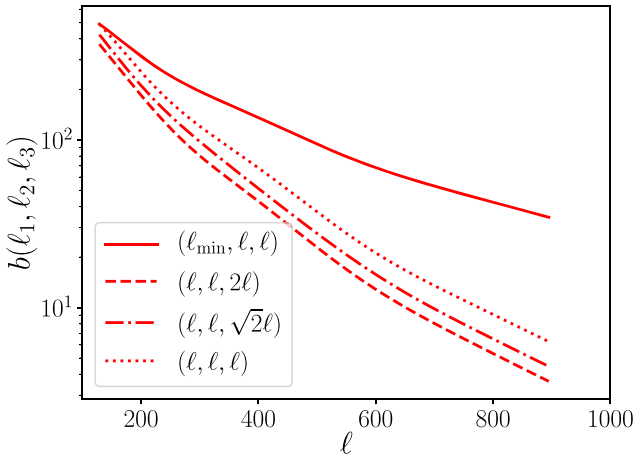

Figure 2. Bispectrum for $\nu_1 = \nu_2 = \nu_3 = 353\,\mathrm{GHz}$ for different triangle configurations without shot noise contribution, which is $b(\ell_1, \ell_2, \ell_3) = b_{1h} + b_{2h} + b_{3h}$. Clearly, the squeezed limit is the dominant contribution for the multipole range shown in the figure.

Since the contamination from Galactic dust is most severe in the Galactic plane, the amplitude of the dust power spectrum strongly depends on the sky fraction, f_{sky} (of the least contaminated pixels) considered. Following Planck Collaboration XXII (2015), Miville-Deschênes et al. (2007), we assume

$$C_\ell^{\mathrm{d}}(\nu_0) = 1.45 \times 10^6 \left(\frac{f_{\mathrm{sky}}}{0.6}\right)^{4.6+7.11\ln(f_{\mathrm{sky}}/0.6)} \ell^{\alpha_{\mathrm{d}}}\,, \tag{33}$$

where α_{d} describes the spatial clustering of the foreground dust. Clearly, a lower frequency coherence will reduce the constraints on these parameters significantly. However, note that, in Planck Collaboration XXII (2015), the dispersion of the dust emissivity index was measured to be 0.07. This corresponds to $\zeta = 10.1$, which yields an almost perfect correlation over the range of frequencies considered here.

Downloaded from https://academic.oup.com/mnras/article-abstract/491/1/1079/5634281 by University of Groningen user on 03 July 2020

Table 2. Frequency bands and the corresponding white noise level w_ν and the angular resolution induced by the beamwidth $\theta_{\rm FWHM}$ for five frequency bands of `Planck` and the frequency bands of `LiteBird` above 200 GHz.

Band ν (GHz)	w_ν (Jy sr^{-1})	$\theta_{\rm FWHM}$ (arcmin)	Experiment
217	43.32	5.02	`Planck`
353	164.7	4.94	
545	185.3	4.83	
857	157.9	4.64	
235	0.36	30.0	`LiteBird`
280	1.45	30.0	
337	1.1	30.0	
402	0.7	30.0	

3 STATISTICS

3.1 Fluctuations in spherical harmonics

We consider $n_{\rm bands}$ maps of CIB intensities, δI_ν, $\nu = \nu_1, ..., \nu_{n_{\rm bands}}$, at frequency ν decomposed into in spherical harmonic coefficients $\delta I_{\ell m,\,\nu}$:

$$\delta I_\nu(\hat{\boldsymbol{n}}) = \sum_{\ell,m} \delta I_{\ell m,\nu} Y_{\ell m}(\hat{\boldsymbol{n}}) \,, \tag{34}$$

where $\hat{\boldsymbol{n}}$ is the direction of the line of sight and $Y_{\ell m}$ are the spherical harmonics. Equation (4) describes the correlation of these modes that have to be diagonal in m and ℓ due to, respectively, the statistical isotropy and homogeneity of the fluctuations.

3.2 Power spectrum

For Gaussian fields, we can express the probability of finding a set of modes $\{\delta I_{\ell m,\,\nu}\}$ given a model $\boldsymbol{\theta}$ by

$$p\left(\left\{\delta I_{\ell m,\nu}\right\}\middle|\boldsymbol{\theta}\right) \propto \prod_\ell \left(\det\left(\boldsymbol{C}_\ell^{-1}\right) \exp\left[\boldsymbol{\delta I}_{\ell m}^\dagger \boldsymbol{C}_\ell^{-1} \boldsymbol{\delta I}_{\ell m}\right]\right)^{2\ell+1} , \tag{35}$$

where we bundled all maps into a vector $\boldsymbol{\delta I}_{\ell m}$. Their covariance is given by $\boldsymbol{C}_\ell = \left\langle \boldsymbol{\delta I}_{\ell m} \boldsymbol{\delta I}_{\ell m}^\dagger \right\rangle$, where the average is applied over all possible realizations of the data. The entries of the covariance are thus given by equation (4). The observed spectra, $\hat{C}_{\ell,\nu\nu'}$ include instrumental noise terms that are given by (Takeuchi & Ishii 2004)

$$\hat{C}_{\ell,\nu\nu'} = C_{\ell,\nu\nu'} + N_\ell(\nu)\delta^{\rm K}_{\nu\nu'} \,, \quad N_\ell(\nu) = w_\nu \exp\left[\ell(\ell+1)\frac{\theta^2_{\rm FWHM}(\nu)}{8\ln 2}\right] \,. \tag{36}$$

Here, w_ν describes the instrumental white noise and $\theta^2_{\rm FWHM}$ the Gaussian beam's width. We summarize the experimental settings in Table 2. The signal-to-noise ratio (SNR) for this set-up is now readily computed as

$$\Sigma^2(\leq \ell_{\rm max}) = f_{\rm sky} \sum_{\ell=\ell_{\rm min}}^{\ell_{\rm max}} \frac{2\ell+1}{2} {\rm tr}\left(\boldsymbol{C}_\ell \hat{\boldsymbol{C}}_\ell^{-1} \boldsymbol{C}_\ell \hat{\boldsymbol{C}}_\ell^{-1}\right) , \tag{37}$$

where $f_{\rm sky}$ is the sky fraction compensating for incomplete sky-coverage. Likewise, the Fisher matrix is given by (Tegmark, Taylor & Heavens 1997)

$$F_{ij}(\boldsymbol{\theta}_0) = f_{\rm sky} \sum_{\ell=\ell_{\rm min}}^{\ell_{\rm max}} \frac{2\ell+1}{2} {\rm tr}\left(\hat{\boldsymbol{C}}_\ell^{-1} \partial_i \boldsymbol{C}_\ell \hat{\boldsymbol{C}}_\ell^{-1} \partial_j \boldsymbol{C}_\ell\right)\Big|_{\boldsymbol{\theta}=\boldsymbol{\theta}_0} , \tag{38}$$

where ∂_i is the derivative with respect to the ith model parameter.

3.3 Bispectrum

The spherical harmonic bispectrum in equation (6) is related to the flat sky bispectrum, $B_{\nu_1,\nu_2,\nu_3}(\boldsymbol{\ell}_1, \boldsymbol{\ell}_2, \boldsymbol{\ell}_3)$, through the relation

$$B_{\nu_1,\nu_2,\nu_3}(\ell_1,\ell_2,\ell_3) \simeq \begin{pmatrix} \ell_1 & \ell_2 & \ell_3 \\ 0 & 0 & 0 \end{pmatrix} \left(\frac{(2\ell_1+1)(2\ell_2+1)(2\ell_3+1)}{4\pi}\right)^{1/2} B_{\nu_1,\nu_2,\nu_3}(\boldsymbol{\ell}_1,\boldsymbol{\ell}_2,\boldsymbol{\ell}_3) \,, \tag{39}$$

i.e. $\boldsymbol{\ell}_i$ are 2D vectors on the flat sky. It is thus consistent with the calculation of the bispectrum, equation (7), which indeed uses the flat sky approximation. The Wigner 3j symbol arises with $m_1 = m_2 = m_3 = 0$ originates from the integration over the Legendre polynomials, ensuring

Downloaded from https://academic.oup.com/mnras/article-abstract/491/1/1079/5634281 by University of Groningen user on 03 July 2020

that the triangular inequality is satisfied. Equation (7) provides an explicit expression for the flat sky bispectrum. Statistical homogeneity is ensured by the fact that the three multipole vectors must form a triangle. We assume a Gaussian covariance for the bispectrum, thus ignoring connected contributions from $n > 2$ correlators. Furthermore, we enforce the condition $\ell_1 \leq \ell_2 \leq \ell_3$ so that each triangle configuration is only counted once. With these approximations, the covariance of the bispectrum takes the simple form

$$\mathrm{Cov}\left[B_{\nu_1\nu_2\nu_3}(\ell_1,\ell_2,\ell_3)B_{\nu_1'\nu_2'\nu_3'}(\ell_1',\ell_2',\ell_3')\right] = \Delta(\ell_1,\ell_2,\ell_3)f_{\mathrm{sky}}^{-1}\left[\hat{C}_{\ell_1,\nu_1\nu_1'}\hat{C}_{\ell_2,\nu_2\nu_2'}\hat{C}_{\ell_3,\nu_3\nu_3'}\right], \tag{40}$$

where $\Delta(\ell_1,\ell_2,\ell_3)$ counts the number of triangular configurations. Note that most of the signal arises from configurations where $\ell_1 \neq \ell_2 \neq \ell_3$, for which $\Delta = 1$.

The SNR for the bispectrum can be calculated as

$$\Sigma^2(\leq \ell_{\mathrm{max}}) = \sum_{\ell_{\mathrm{min}}\leq\ell_1\leq\ell_2\leq\ell_3}^{\ell_{\mathrm{max}}} \boldsymbol{B}^T(\ell_1,\ell_2,\ell_3)\boldsymbol{C_B}^{-1}(\ell_1,\ell_2,\ell_3)\boldsymbol{B}(\ell_1,\ell_2,\ell_3)\,, \tag{41}$$

where, again, we bundled all the bispectra $B_{\nu_1,\nu_2,\nu_3}(\ell_1,\ell_2,\ell_3)$ at a single multipole combination into the vector $\boldsymbol{B}(\ell_1,\ell_2,\ell_3)$, with the ordering $\nu_1 \leq \nu_2 \leq \nu_3$. The covariance matrix $\boldsymbol{C_B}$ is the bundled version of equation (40). As a result, the Fisher matrix assumes the following form:

$$F_{ij}(\boldsymbol{\theta}_0) = \sum_{\ell_{\mathrm{min}}\leq\ell_1\leq\ell_2\leq\ell_3}^{\ell_{\mathrm{max}}} \partial_i\boldsymbol{B}^T(\ell_1,\ell_2,\ell_3)\boldsymbol{C_B}^{-1}(\ell_1,\ell_2,\ell_3)\partial_j\boldsymbol{B}(\ell_1,\ell_2,\ell_3)\big|_{\boldsymbol{\theta}=\boldsymbol{\theta}_0}\,. \tag{42}$$

For the sake of computational tractability, we will bin the summation in the outer two sums over the ℓ-modes and only apply the full sum for ℓ_3 to take into account the correct behaviour of the Wigner 3j symbol.

3.4 Experimental setting and foreground modelling

The choice of frequency bands, along with the white noise level and the resolution, are all listed in Table 2. For the sky fraction, we assume $f_{\mathrm{sky}} = 0.6$ that will be used as the default value from now on unless stated otherwise.

The most challenging step in reconstructing maps of the CIB is the removal of contaminating signals such as the CMB or Galactic dust (Planck Collaboration XIII 2013; Planck Collaboration XLVIII 2016; Lenz, Doré & Lagache 2019). The CMB signal can be extracted easily owing to its blackbody nature, provided that the frequency coverage is sufficient. We will thus assume that the CMB has already been removed from the maps. For Galactic dust emission, the situation is much more involved. In principle, there are two approaches to deal with foreground contaminants: (i) include the dust model in the likelihood analysis; or (ii) remove the dust from the CIB maps. For the second case, Tucci et al. (2016) used a method very similar to the ones used for CMB reconstruction (Tucci et al. 2005; Stompor et al. 2009; Stivoli et al. 2010; Errard et al. 2016). They showed that high frequencies are of paramount importance for a successful reconstruction of CIB maps. The reason for this is that the CIB and Galactic dust SEDs, equations (27) and (30), have very similar shape and differ only at higher frequencies. For this kind of CIB reconstruction, the noise variance of the CIB maps is given by

$$\Sigma^2_{\mathrm{CIB}}(\nu) = \frac{\sum_i \Theta^2_{\mathrm{d}}(i)/\sigma_i^2}{\det(\boldsymbol{A}^T\boldsymbol{N}^{-1}\boldsymbol{A})}\,, \tag{43}$$

where $\boldsymbol{A}$ is the mixing matrix that describes how the two components (CIB and Galactic dust) mix in different frequency bands. $\boldsymbol{N}$ is the noise covariance matrix. The reconstruction strategy then works as follows: Given a survey with N_ν frequencies, $N_\nu/2$ are used for the reconstruction, while the remaining channels are used for the CIB measurement. The reconstruction noise is then given by equation (43) that adds to the observed spectrum. In reality, there may be dust residuals in the CIB maps after the reconstruction. Furthermore, the reconstruction may also remove signal from the CIB itself owing to the very similar shape of the SEDs. We will ignore the latter effect in the following, but one should bear in mind that this could be an important source of systematics.

The SNR for the power spectrum and the bispectrum is shown in the left-hand and right-hand panel of Fig. 3, respectively. We assume a fully reconstructed CIB in eight frequency bands. This means that we used another eight frequency bands, which are not shown in the analysis, to remove the galactic dust. The resulting reconstruction noise is assumed to be subdominant on the scales shown in the plot. Different colours indicate the amount of residual Galactic dust contribution in the power spectrum and bispectrum. In the left-hand panel, the solid lines show the cumulative SNR, while the dashed lines correspond to the SNR contribution at each multipole. The position of the kink in the dashed curves corresponds to the angular resolution of `LiteBird`. It should be noted that the SNR is still rising at $\ell > 10^3$. However, as seen in Fig. 1, the spectra are dominated by the shot noise contribution that itself carries very few information about cosmology, and is mainly sourced by the scatter in the M–L relation. The right-hand panel shows only the cumulative SNR for the bispectrum. Clearly, it is dominated by the noise on angular scales smaller than the power spectrum. Furthermore, the total CIB bispectrum signal strength is approximately four times smaller than that of the power spectrum.

The second possibility is to fit all the components separately. In particular, we can write the observed signal as

$$\delta I_\nu(\hat{\boldsymbol{n}}) = \delta I_\nu^{\mathrm{CIB}}(\hat{\boldsymbol{n}}) + \delta I_\nu^{\mathrm{SN}}(\hat{\boldsymbol{n}}) + \delta I_\nu^{\mathrm{d}}(\hat{\boldsymbol{n}})\,, \tag{44}$$

Downloaded from https://academic.oup.com/mnras/article-abstract/491/1/1079/5634281 by University of Groningen user on 03 July 2020

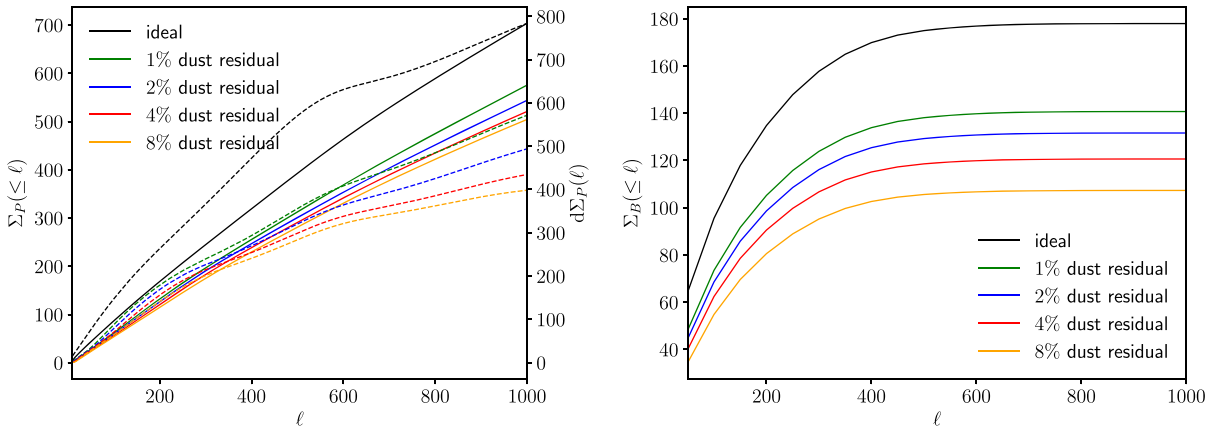

Figure 3. Signal-to-noise ratio (SNR) for CIB maps whose noise is given only by instrumental noise, cosmic variance, and possibly residual dust. *Left*: Cumulative SNR of a power spectrum as the solid lines, while the dashed lines correspond to the differential SNR. *Right*: Cumulative SNR for a bispectrum measurement.

for CIB clustering, shot noise, and the dust component, respectively. In harmonic space, we obtain a similar splitting on the power spectra level since the different signals are spatially uncorrelated:

$$\hat{\boldsymbol{C}}(\ell) = \boldsymbol{C}_{\rm CIB}(\ell) + \boldsymbol{N}(\ell) + \boldsymbol{C}_{\rm d}(\ell)\,, \tag{45}$$

where the first to terms are given by equation (36) plus the shot noise contribution and the last term by equation (33). A similar equation can be found for higher order spectra.

4 RESULTS

In this section, we discuss the constraining power of CIB measurements on cosmological and HOD parameters in the absence and presence of foregrounds. The power spectrum and bispectrum analysis is discussed separately. Finally, we also describe the combination of power and bispectrum. Throughout this section, we use the experimental settings specified in Table 2 with a sky-fraction $f_{\rm sky} = 0.6$.

4.1 Power spectrum

First, we are interested in the sensitivity of the experiment described in Table 2 for the case where we fit all components simultaneously as outlined in the previous section. To this end, we fit all the components at the power spectrum and bispectrum level, rather than at the map level. In particular, we fix the slope $\alpha_{\rm d}$ and fit for a free dust amplitude at each frequency. We thus allow for slightly more flexibility in the SED modelling and, at the same time, ensure that the correlations are still described by equation (32). For the dust component, we therefore have N_ν free parameters. The shot noise is fitted in each of the $N_\nu(N_\nu+1)/2$ pairs of frequency band separately, subject to satisfy the Cauchy–Schwarz inequality. This is very similar to the procedure outlined in Feng et al. (2018). This amounts to $N_\nu(N_\nu+1)/2$ additional parameters. The clustering signal of the CIB is fitted by varying both the CIB and cosmological parameters. This includes the total mass $\sum m_\nu$ of neutrinos, which reduce the small-scale clustering amplitude. We have consistently taken into account the impact of the resulting scale-dependent growth (Bond, Efstathiou & Silk 1980) on the linear power spectrum and on the halo mass function through the variance, equation (22; Saito, Takada & Taruya 2009; Ichiki & Takada 2012; Castorina et al. 2014). In particular, the cold dark matter density gets reduced to

$$\Omega_{\rm cdm} \equiv \Omega_{\rm m} - \Omega_{\rm b} - \frac{\sum m_\nu}{93.14h^2}\,, \tag{46}$$

with the mass of the neutrinos in eV.

In Fig. 4, we show the cumulative sensitivity (i.e. the Fisher information), equation (38), up to multipole ℓ marginalized over the shot noise and dust parameters. The sensitivity saturates above $\ell \approx 10^3$ due to the shot noise being the dominating contribution. Since the shot noise merely acts as a nuisance parameter in our model, we will restrict our analysis to $\ell \leq 10^3$ from now on. Depending on the focus of the analysis, however, digging into the shot noise at higher multipoles may provide additional information about the physical modelling of the CIB (Shang et al. 2012; Lacasa et al. 2014; Pénin et al. 2014). For the minimum multipole, we choose a conservative value of $\ell_{\rm min} = 50$ to reduce the contamination by foregrounds.

Fig. 5 shows a triangle plot with the 1σ contours. Only measurements at multipoles $50 < \ell < 1000$ have been considered, and the general settings described in Table 2 has been used. The black and red ellipses show the constraints when the dust has been completely removed, or cleaned at the 92 per cent level, respectively. The blue ellipses correspond to the case where the dust and shot noise components have been marginalized over. Clearly, the impact of the dust residuals and the $N_\nu(N_\nu+1)/2$ additional shot noise amplitudes strongly reduces the

Downloaded from https://academic.oup.com/mnras/article-abstract/491/1/1079/5634281 by University of Groningen user on 03 July 2020

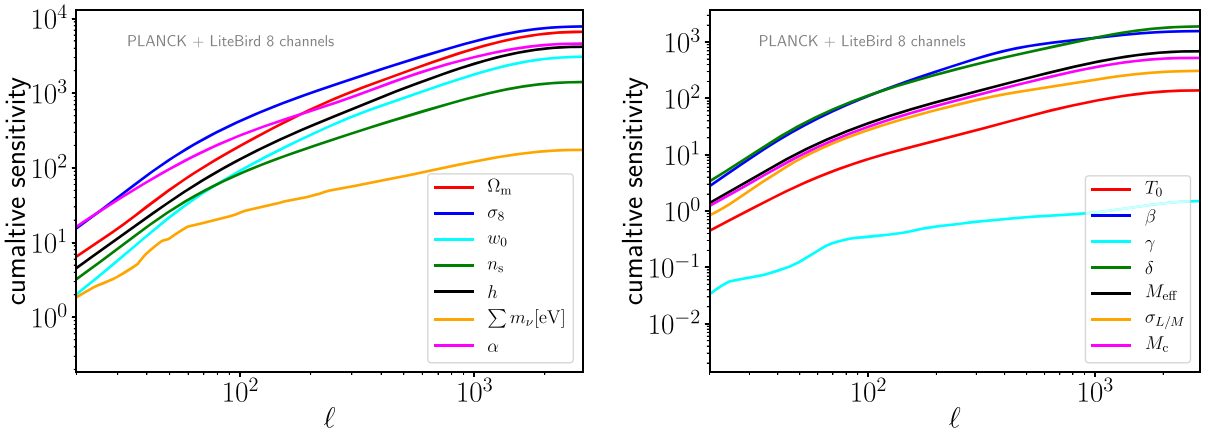

Figure 4. Cumulative sensitivity of the power spectrum marginalized over the shot noise and dust contributions as a function of multipole ℓ. That is, we sum up equation (38) up to multipole ℓ. The Fisher matrix is still conditionalized on the cosmological, HOD, and CIB parameters, thus they are still fixed to their respective fiducial values. The experimental settings are summarized in Table 2. *Left*: sensitivity om cosmological parameter *Right*: sensitivity on HOD and CIB parameters.

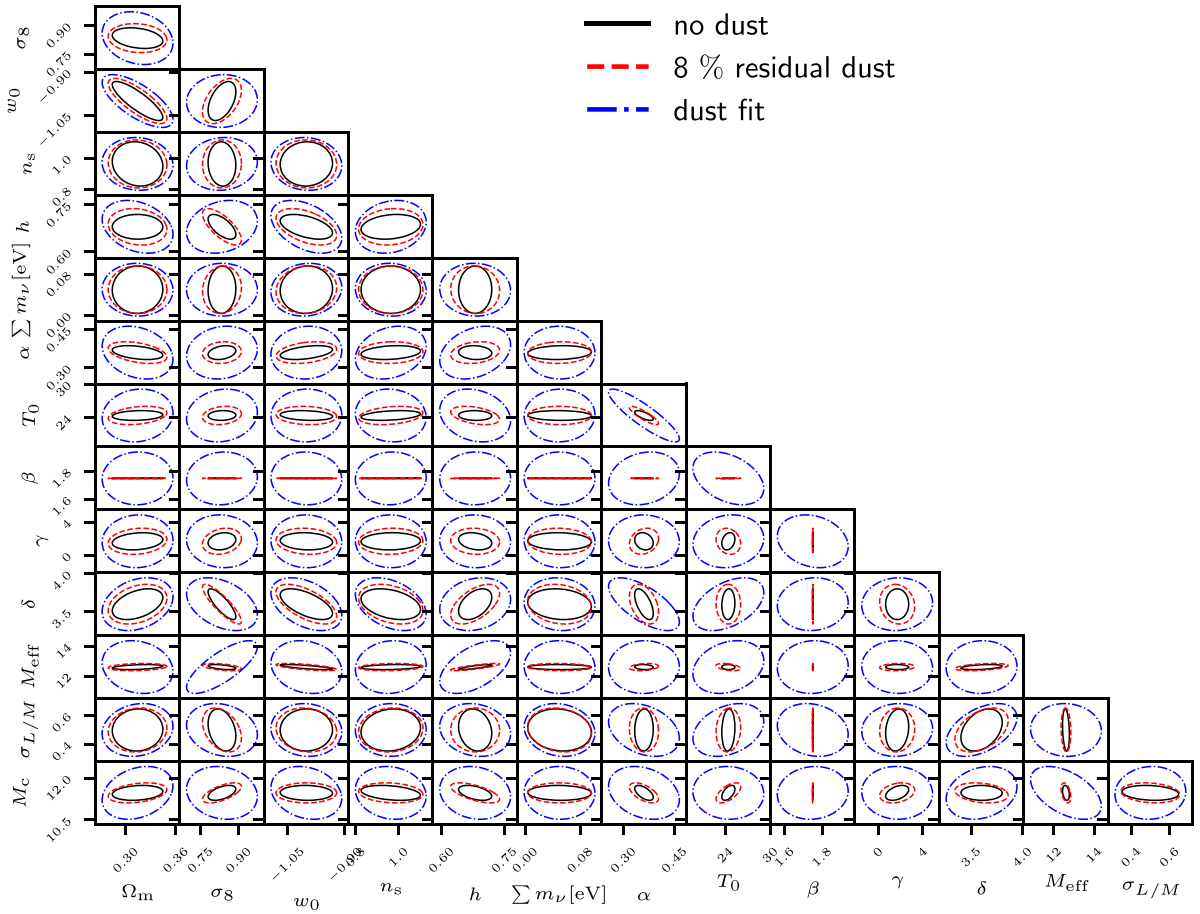

Figure 5. 1σ constraints on CIB and cosmological parameters for the survey described in Table 2 using the power spectrum only with a sky fraction of 60 per cent. The multipole range considered is $\ell \in [50, 1000]$. The sold black ellipses correspond to an ideal CIB survey without any dust residuals, while the dashed red ellipses have 8 per cent dust residual at the power spectrum level. The blue dash–dotted ellipses fit the dust component and marginalize over it.

Downloaded from https://academic.oup.com/mnras/article-abstract/491/1/1079/5634281 by University of Groningen user on 03 July 2020

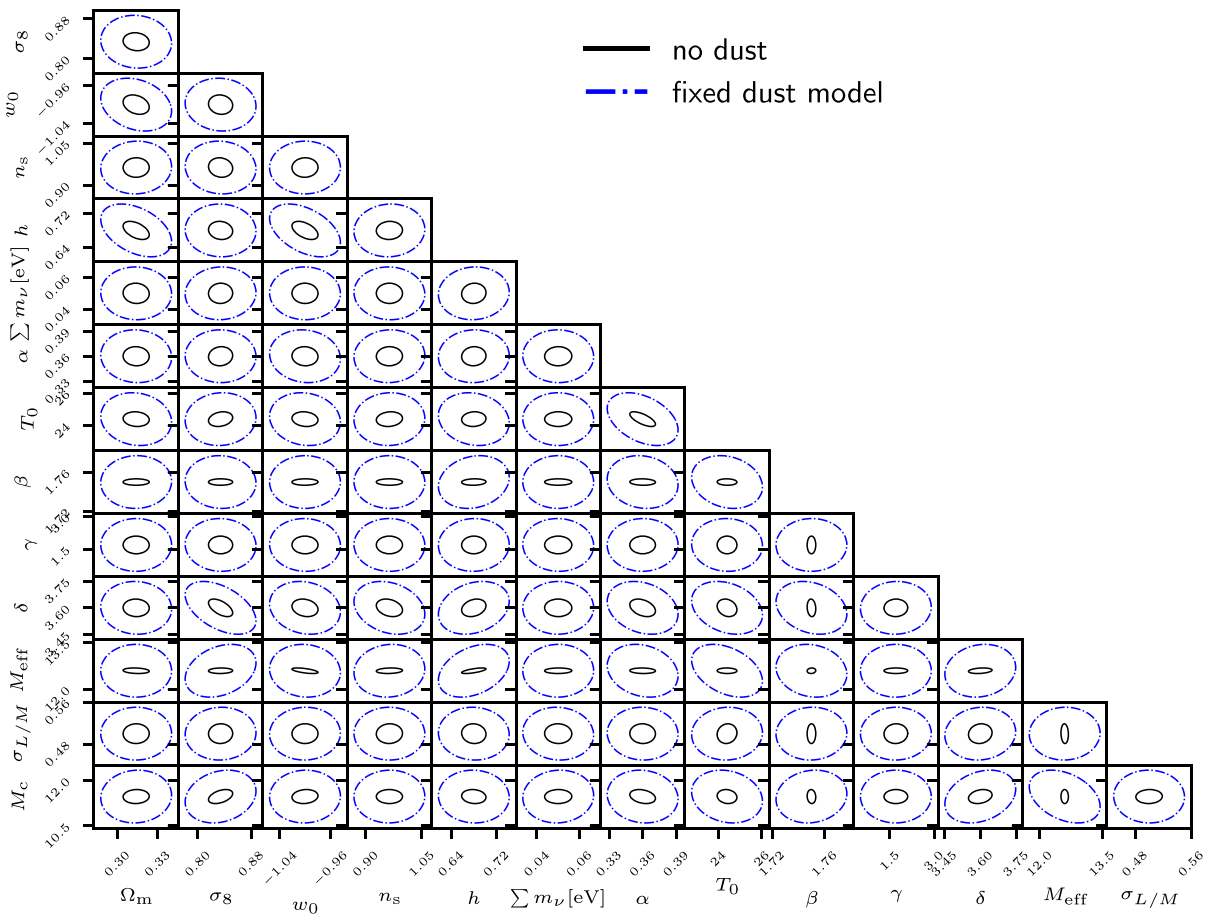

Figure 6. Marginal contours for cosmological, CIB, and HOD parameters using the survey settings described in Table 2. The black solid ellipses show the constraints from the bispectrum without any galactic dust residuals present in the survey. The dash–dotted blue ellipses show the constraints when it is still fully present in the survey as a noise source but where the dust model has not been marginalized over. The multipole range considered is $\ell \in [50, 1000]$ and the sky fraction is 60 per cent.

possible constraints on the CIB and HOD parameters. Interestingly, the cosmological parameters are largely unaffected. This result depends slightly on the fact that we assume a fixed power law for the spatial correlations of the foreground dust. However, even if this assumption is relaxed, the overall loss in precision is rather small. The amplitude of the power spectrum, σ_8, experiences the largest loss in precision. For the CIB parameters, the biggest effect can be seen for β. This can be understood from the fact that β is strongly degenerated with the dust, since it describes the modification to the blackbody spectrum of the CIB and therefore can be constrained precisely with aid of different frequency channels and their cross-correlations. One would, in principle, expect a similar effect for the high-frequency power-law slope of the CIB's SED. However, most of the frequencies considered here lie below the peak of the SED across most of the redshift range probe by the CIB. This is the reason why it remains largely unconstrained. Overall, large effects can be seen for all parameters associated with the infrared luminosity of the galaxies (equation 26) with the exception of $\sigma_{L/M}$. One could also allow for the amplitude of the CIB power spectrum to vary with frequency. This would increase the errors on the SED parameters even further. However, the constraints on the cosmological parameters would be unchanged.

4.2 Bispectrum

Before we present the results for the Fisher analysis of the bispectrum, we stress again that we do not consider contributions to the covariance from the 3 −, 4 −, or 6 −point correlation functions. Consequently, we likely underestimate the actual noise level. None the less, note that the term C_ℓ^3 dominates the terms stemming from B_ℓ^2 at most angular scales. The individual contributions to the covariance equation (40) are, again, given by the cosmic variance of the CIB, Galactic dust, shot noise, and instrumental noise. Although the bispectrum is measured with less significance than the power spectrum, its sensitivity to non-linear parameters can be much higher, resulting into tighter constraints. Moreover, parameter degeneracies can be very different compared to an analysis of the power spectrum solely.

Fig. 6 shows the 1σ error contours for a bispectrum analysis in which Galactic dust has been fully removed (black), and in which the dust is still present as noise (black). Comparing this to the results obtained for the power spectrum, we see that any residual dust affects most

Downloaded from https://academic.oup.com/mnras/article-abstract/491/1/1079/5634281 by University of Groningen user on 03 July 2020

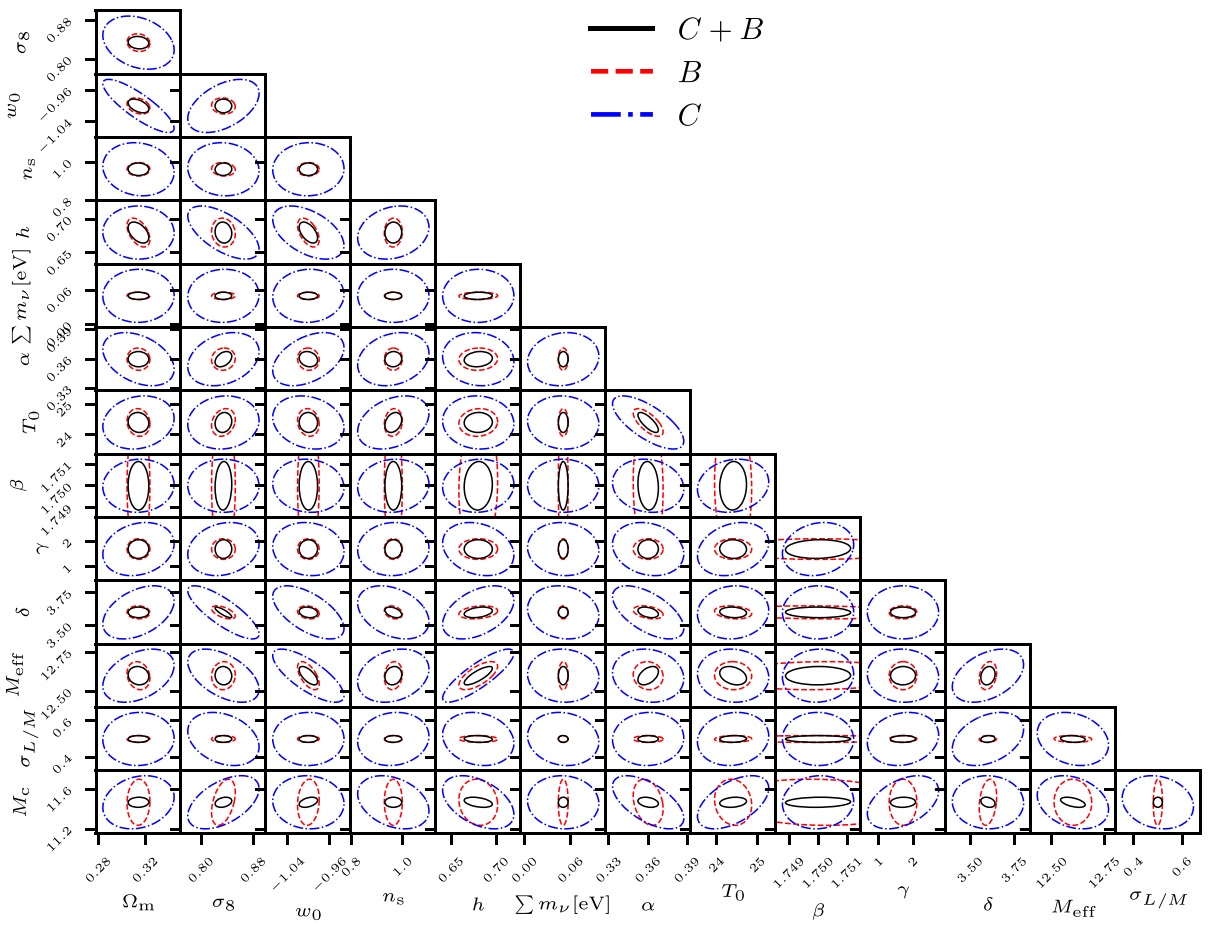

Figure 7. Marginal contours for cosmological, CIB, and HOD parameters using the survey settings described in Table 2. The red dashed ellipses show the constraints from the bispectrum alone, while the blue dash–dotted ellipses correspond to the dashed black contours in Fig. 5. The solid black ellipses show the constraints from the combination of the power spectrum and the bispectrum analysis. The multipole range considered is $\ell \in [50, 1000]$ and the sky fraction is 60 per cent.

parameters equally, with β and M_eff being exceptions. The reason is twofold: the overall noise in the bispectrum analysis is higher, and most of the signal originates from smaller angular scales where the dust dominates (compare the panels of Fig. 3).

In order to compare the power spectrum and the bispectrum analysis, we show in Fig. 7 the 1σ contours for both analysis when the CIB maps are assumed to be dust free. Furthermore, the result of a combined analysis is shown in black. For the latter, the bispectrum and power spectrum have been treated as two independent probes. Since the covariance between the two probes has no Gaussian contribution, the autocorrelations in the covariance are expected to dominate the cross-correlations, which justifies our assumptions. The marginal constraints of this figure are summarized in Table 3. Clearly, the power spectrum is outperformed by the bispectrum for the cosmological parameters, usually yielding a factor 3−4 improvement. The biggest improvement arises for the sum of the neutrino masses. Interestingly, we find that the degeneracy directions are quite similar for the cosmological parameters. Consequently, the combination of power spectrum and bispectrum does not yield a substantial improvement for these parameters. The situation is very similar for the HOD and CIB parameters. However, it is possible to break degeneracies including M_c that yields much tighter constraints for M_c when combining both probes (cf. Table 3).

5 CONCLUSIONS

In this paper, we investigated the information content of CIB anisotropies using their power and bispectrum. Previous work (Pénin et al. 2014) mainly focused on the impact of the HOD parameters, mass function, and galaxy formation on the CIB's bispectrum. Further work used the CIB at large scales to constrain the star formation rate, the CIB's effective bias as well as the dark matter mass of star-forming galaxies (Maniyar et al. 2018). Similarly, (Maniyar et al. 2019) applied cross-correlation of the CIB with the integrated Sachs–Wolfe effect to constrain dark energy. Our approach is complementary since we investigate the information content of the CIB also with respect to the cosmological parameters, exploiting multiple frequency bands, and their cross-correlations.

We analytically modelled the anisotropies using the halo model and the approach introduced in Shang et al. (2012). In particular, the model assumes that the clustering of haloes on large scales is reasonably described by the combination of the halo model with a HOD. Each

Downloaded from https://academic.oup.com/mnras/article-abstract/491/1/1079/5634281 by University of Groningen user on 03 July 2020

Table 3. Marginal constraints for cosmological, CIB, and HOD parameters using the survey settings described in Table 2. The first two columns display the constraints obtained from the power spectrum and the bispectrum, respectively. The third column summarizes the per cental change of the constraints. The last columns give the error achievable with a joint analysis of the CIB power spectrum and bispectrum. For all absolute errors, the relative error is shown in per cent in brackets.

Parameter	σ_C	σ_B	σ_{C+B}
Ω_m	0.0201 (6.39)	0.0064 (2.05)	0.0058 (1.85)
σ_8	0.0361 (4.33)	0.0120 (1.44)	0.0084 (1.01)
w_0	0.0449 (4.49)	0.0136 (1.36)	0.0116 (1.16)
n_s	0.0919 (9.55)	0.0232 (2.41)	0.0217 (2.25)
h	0.0262 (3.85)	0.0142 (2.09)	0.0103 (1.52)
$\sum m_\nu$[eV]	0.0307 (61.39)	0.0042 (8.47)	0.0042 (8.38)
α	0.0181 (5.02)	0.0076 (2.10)	0.0052 (1.44)
T_0	0.5771 (2.37)	0.3007 (1.23)	0.2169 (0.89)
β	0.0008 (0.05)	0.0022 (0.12)	0.0007 (0.04)
γ	0.6877 (40.45)	0.2671 (15.71)	0.2422 (14.25)
δ	0.1337 (3.71)	0.0327 (0.91)	0.0267 (0.74)
M_eff	0.1122 (0.89)	0.0593 (0.47)	0.0387 (0.31)
$\sigma_{L/M}$	0.0972 (19.44)	0.0125 (2.50)	0.0123 (2.47)
M_c	0.1771 (1.54)	0.1537 (1.34)	0.0336 (0.29)

galaxy is then assigned a specific IR emissivity, which is fully specified by the SED and by a mean mass–luminosity relation. We did not explicitly model the shot noise contribution, which can be done with empirical models (Béthermin et al. 2011; Wu & Doré 2017). Overall, our phenomenological model is sufficient for the multipole range considered here, although it would be desirable to phrase it as a rigorous bias expansion (Desjacques, Jeong & Schmidt 2018).

The theoretical predictions were applied to forecast constraints on HOD, CIB, and cosmological parameters for a combined survey of *Planck* and LiteBird with a total of eight frequency channels between 200 and 900 GHz, using all the autoorrelation and cross-correlation available. Furthermore, we studied the impact of Galactic dust emission that we assumed to be strongly correlated over the relevant range of frequencies, and whose angular power spectrum was modelled as a power law. In particular, we investigated the impact of dust residuals on the constraints yielded by the power spectrum. Furthermore, we explore the sensitivity of the bispectrum, and of its combination with the power spectrum, to the model parameters. We summarize our main results as follows:

(i) For the experiments considered here, the power spectrum CIB signal of the clustering component can be measured by a few hundred σ when the foreground dust is at least partially removed (with a maximum of 8 per cent dust residuals). For the bispectrum, the SNR is roughly four times smaller.

(ii) Confidence intervals on cosmological parameters are not strongly affected by residual dust in the maps. Even if the dust model and the shot noise are treated as free parameters, the cosmological parameters are still constrained down to an uncertainty of ~ 10 per cent even after marginalization. In a different setting, Maniyar et al. (2019) found that the dust has to be removed to the 0.01 per cent level when cross-correlating the CIB with CMB temperature fluctuations on large scales.

(iii) The clustering components (i.e. all at least partially connected parts of the correlation functions) of the bispectrum suffer more strongly from residual dust, since the shot noise component becomes important at lower multipoles, where the dust contribution is more dominant.

(iv) Overall the power spectrum yields weaker constraints (by a factor of 4) than the bispectrum for almost all parameters of the model – assuming that both the power spectrum and bispectrum model are equally accurate over the multipole range considered. Degeneracy directions are very similar between the power spectrum and the bispectrum analysis. Therefore, the combination of both statistics yields substantial improvement for the HOD parameters solely. However, we caution that this might be due to the simplified bias description generally adopted in such halo model approaches.

We plan to refine the halo model description of the CIB by including other relevant terms from the bias expansion and, possibly, taking into account scatter in the HOD parameters to model better the shot noise. Further analysis could include a study of the cross-correlation between CIB and LSS probes – such as spectroscopic galaxy surveys like SPHEREx (Doré et al. 2014) – which can probe a similar redshift range; and an application of CIB bispectrum measurements to constrain primordial non-Gaussianities.

ACKNOWLEDGEMENTS

RR and VD acknowledges support by the Israel Science Foundation (grant no. 1395/16). RR and SZ furthermore acknowledge support by the Israel Science Foundation (grant no. 255/18).The authors thank Tsutomu T. Takeuchi for comments on the draft.

Downloaded from https://academic.oup.com/mnras/article-abstract/491/1/1079/5634281 by University of Groningen user on 03 July 2020

REFERENCES

Béthermin M., Dole H., Lagache G., Le Borgne D., Penin A., 2011, A&A, 529, A4
Bond J. R., Efstathiou G., Silk J., 1980, Phys. Rev. Lett., 45, 1980
Castorina E., Sefusatti E., Sheth R. K., Villaescusa-Navarro F., Viel M., 2014, J. Cosmol. Astropart. Phys., 2014, 049
Cooray A., Sheth R., 2002, Phys. Rep., 372, 1
Desjacques V., Jeong D., Schmidt F., 2018, Phys. Rep., 733, 1
Doré O. et al., 2014, preprint (astro-ph/1412.4872)
Dwek E. et al., 1998, ApJ, 508, 106
Errard J., Feeney S. M., Peiris H. V., Jaffe A. H., 2016, J. Cosmol. Astropart. Phys., 2016, 052
Feng C., Cooray A., Bock J., Chang T.-C., Doré O., Santos M. G., Silva M. B., Zemcov M., 2019, ApJ, 875, 86
Fixsen D. J., Dwek E., Mather J. C., Bennett C. L., Shafer R. A., 1998, ApJ, 508, 123
Hall N. R. et al., 2010, ApJ, 718, 632
Ichiki K., Takada M., 2012, Phys. Rev. D, 85, 063521
Lacasa F., Pénin A., Aghanim N., 2014, MNRAS, 439, 123
Lagache G., Bavouzet N., Fernandez-Conde N., Ponthieu N., Rodet T., Dole H., Miville-Deschênes M.-A., Puget J.-L., 2007, ApJ, 665, L89
Lazeyras T., Wagner C., Baldauf T., Schmidt F., 2016, J. Cosmol. Astropart. Phys., 2016, 018
Lenz D., Doré O., Lagache G., 2019, ApJ, 883, 75
Lesgourgues J., 2011, preprint (astro-ph/1104.2932)
Limber D. N., 1954, ApJ, 119, 655
Maniyar A., Lagache G., Béthermin M., Ilić S., 2019, A&A, 621, A32
Maniyar A. S., Béthermin M., Lagache G., 2018, A&A, 614, A39
Miville-Deschênes M.-A., Lagache G., Boulanger F., Puget J.-L., 2007, A&A, 469, 595
Navarro J. F., Frenk C. S., White S. D. M., 1997, ApJ, 490, 493
Pénin A. et al., 2012, A&A, 543, A123
Pénin A., Lacasa F., Aghanim N., 2014, MNRAS, 439, 143
Planck Collaboration XVIII, 2011, A&A, 536, A18
Planck Collaboration XIII, 2013, A&A , 571, A13
Planck Collaboration XXX, 2014, A&A, 571, A30
Planck Collaboration XXII, 2015, A&A, 576, A107
Planck Collaboration XLVIII, 2016, A&A, 596, A109
Planck Collaboration, 2018, preprint (astro-ph/1807.06209)
Saito S., Takada M., Taruya A., 2009, Phys. Rev. D, 80, 083528
Shang C., Haiman Z., Knox L., Oh S. P., 2012, MNRAS, 421, 2832
Stivoli F., Grain J., Leach S. M., Tristram M., Baccigalupi C., Stompor R., 2010, MNRAS, 408, 2319
Stompor R., Leach S., Stivoli F., Baccigalupi C., 2009, MNRAS, 392, 216
Takeuchi T. T., Ishii T. T., 2004, ApJ, 604, 40
Tegmark M., 1998, ApJ, 502, 1
Tegmark M., Taylor A. N., Heavens A. F., 1997, ApJ, 480, 22
Tinker J., Kravtsov A. V., Klypin A., Abazajian K., Warren M., Yepes G., Gottlöber S., Holz D. E., 2008, ApJ, 688, 709
Tinker J. L., Wetzel A. R., 2010, ApJ, 719, 88
Tucci M., Martínez-González E., Vielva P., Delabrouille J., 2005, MNRAS, 360, 935
Tucci M., Desjacques V., Kunz M., 2016, MNRAS, 463, 2046
Viero M. P. et al., 2009, ApJ, 707, 1766
4Viero M. P. et al., 2012, MNRAS, 421, 2161
Wu H.-Y., Doré O., 2017, MNRAS, 466, 4651

This paper has been typeset from a TEX/LATEX file prepared by the author.

Downloaded from https://academic.oup.com/mnras/article-abstract/491/1/1079/5634281 by University of Groningen user on 03 July 2020